ORIGINAL PAPER

A study on the supercapacitive behavior of zinc substituted manganese ferrite nanoparticles

A. Ghasemi[1,2] · M. Kheirmand[1] · H. Heli[2]

Abstract

Synthesis and applications of novel nanomaterials in energy storage are of great importance. In this study, nanoparticles of zinc substituted manganese ferrite ($Zn_{0.5}Mn_{0.5}Fe_2O_4$) were synthesized by a simple coprecipitation method. The synthesized nanoparticles were then characterized by field emission scanning electron microscopy, FTIR spectroscopy, atomic force microscopy and X-ray diffraction. The nanoparticles had a spherical morphology with a diameter of ~ 30 nm. The nanoparticles were electrochemically evaluated as a supercapacitor electrode material by cyclic voltammetry, electrochemical impedance spectroscopy and charge/discharge cycling. The nanoparticles represented both double layer and pseudocapacitive behaviors with a specific capacitance of 77.9 F g^{-1} at a charge/discharge current of 1.0 A g^{-1}. The specific energy and power of the nanoparticles were 13.2 Wh g^{-1} and 563 W g^{-1}, respectively. The nanoparticles retained more than 87% of the initial capacitance after 1000 charge/discharge cycles.

Keywords Supercapacitor · Substituted ferrite · Magnetic nanoparticles · Pseudocapacitor

Introduction

Over the past years, considerable researches have been performed for the development of energy storage devices with high power densities as environmentally clean energy systems [1, 2]. These devices are especially interested in recent years for miniaturized, lightweight portable, hybrid electric and wireless electronic devices. Supercapacitors with a high power output, huge cyclability and short recharge time are promising energy devices for application in integrated power systems [3–7]. Supercapacitors store energy through specific ionic adsorption (double layer supercapacitors) or both ionic adsorption and reversible faradaic processes (pseudocapacitors). These devices are environmental friendly and have almost independent operation from ambient temperature and very safe, so they are desirable in electronics, transportation, communication and aviation applications. For the development of these devices, design and synthesis of new electrode materials with high energy density, long cycle life and higher power are interested. Furthermore, enhancement the power density is necessitated to increase the kinetics of electron and ion transport in electrodes and at the electrode/electrolyte interface. For increase energy density, optimizations of the design of electrode material and its structure with accordance with energy storage mechanisms have to been considered [4]. In this regard, different materials of metal oxides [8–10], conducting polymers [6, 11, 12], proteins [13, 14], graphene [15] and its composites [6, 7, 16, 17] and transition metal hexacyanoferrates [5] have been approached.

Spinel transition metal ferrites (MFe_2O_4, M=Ni^{2+}, Mn^{2+}, Zn^{2+}, or Co^{2+}) have attracted much attentions as promising materials due to low saturation magnetic moment, low cost, ecofriendly, electrical properties, thermal stability, and chemical manipulation ability [18, 19]. These materials, especially in nano-size dimensions, have potential applications in vast areas of magnetic resonance imaging [20], drug delivery [21–23], biosensors [24], dielectric materials [25], bioseparation [26], electrocatalysis [27], Li-batteries [28], and supercapacitors [29, 30]. Up to now, different ferrites have been applied to fabricate supercapacitors. Among the ferrites, ferrites of nickel [29–36], manganese [37–43], zinc

✉ M. Kheirmand
  kheirmand@gmail.com

✉ H. Heli
  hheli7@yahoo.com; heli@sums.ac.ir

1   Department of Chemistry, School of Basic Sciences, Yasouj University, Yasouj, Iran

2   Nanomedicine and Nanobiology Research Center, Shiraz University of Medical Sciences, Shiraz, Iran

[44, 45], cobalt [46–49], copper [50–53], and aluminum [54, 55] have been employed. In Table 1, different ferrites employed for the fabrication of supercapacitors and their capacitances are summarized. Based on the information, the supercapacitive behavior of ferrites depends on type of ferrite, substitution with transition metal ions, level of substitution, and other compounds employed along with the ferrites.

In the present study, nanoparticles of $Zn_{0.5}Mn_{0.5}Fe_2O_4$ (ZMFNPs) were synthesized by a simple coprecipitation route, characterized and then applied as a supercapacitor electrode material.

Experimental section

Materials

All chemicals were purchased form Merck (Germany) and used without further purification. Redistilled water was used throughout the study.

Synthesis of ZMFNPs

ZMFNPs were synthesized by an aqueous coprecipitation route. Zinc, manganese, and iron (III) chlorides with the appropriate stoichiometric proportions were dissolved in a dilute hydrochloric acid solution of 0.1 mol L^{-1}, and warm to 80 °C. A sodium hydroxide solution of 4 mol L^{-1} was prepared separately and warm to 80 °C. These warm solutions were then rapidly mixed with magnetic stirring and the final pH was set at 12.0. Then, the temperature was raised creased to 100 °C and stirring was continued for 1 h for crystallization of ZMFNPs. Afterward, the mixture was cooled to room temperature, the precipitate was collected by a permanent magnet, and washed several times with water to neutralize the supernatant. ZMFNPs were dried at room temperature.

Apparatus

Electrochemical experiments were performed in a three-electrode cell with 0.05 KOH solution or a symmetrical two-electrode cell powered by a ∝-Autolab potentiostat/galvanostat, type III, FRA2 (The Netherlands). An Ag/AgCl, 3 mol L^{-1} KCl and a platinum plate were used as the reference and counter electrodes, respectively. The system was run on a PC through GPES and FRA 4.9 softwares. Electrochemical characteristics of ZMFNPs were investigated by cyclic voltammetry, charge/discharge and electrochemical impedance spectroscopy (EIS) measurements. For EIS, a frequency range 100 kHz to 25 mHz with an ac voltage amplitude of 10 mV and an equilibrium time of 5 s were employed.

Field emission scanning electron microscopy (FESEM) was performed using a Zeiss, Sigma-IGMA/VP (Germany) equipped with energy-dispersive X-ray spectroscopy. Atomic force microscopy (AFM) was performed by a Nano Wizard 108 II, JPK instrument (Germany) in the non-contact mode by a standard silicon tip at room temperature. FTIR spectra were acquired to investigate the nature of the formed chemical bonds by a Bruker Tensor 27 spectrometer. X-ray diffraction (XRD) patterns were recorded using a Philips X'Pert diffractometer (the Netherlands) equipped with a Cu/K_{α} radiation source at a scanning rate of 1° min^{-1} in a 2θ range of 15°–90°.

Preparation of electrodes

Preparation of the working electrodes for three-electrode cell

A glassy carbon (GC) electrode of 2 mm diameter was firstly polish on a polishing pad using 0.05 ∝m alumina powder lubricated by water and then ultrasonicated in an ultrasound bath in a water:ethanol mixture (1:3 V/V). The electrode was then used directly, covered by acetylene black (GC/AB electrode), or covered with a mixture of acetylene black and ZMFNPs (NC electrode). For preparation of the GC/AB electrode, a mixture of 66 wt% acetylene black and 34 wt% polyvinylidene difluoride was prepared and N-methyl-2-pyrrolidinone was added to form slurry. The weight of active materials was 0.06 mg. Then, the slurry was cast on the GC electrode and left to dry at 60 °C for 24 h. For preparation of the NC electrode, a mixture of 80 wt% of ZMFNPs, 15 wt% acetylene black and 5 wt% polyvinylidene difluoride was prepared and N-methyl-2-pyrrolidinone was added to form slurry. The weight of active materials was 0.1 mg. Then, the slurry was cast on the GC electrode surface and left to dry at 60 °C for 24 h. It should be noted that for preparation of the NC electrode, AB was employed to improve the electrical conductivity of ZMFNPs and to better adherence of the active material into the GC electrode surface.

Preparation of electrodes for two-electrode cell

For the charge/discharge measurements of the two-electrode symmetric cell, graphite plate substrates were first polished with ultrafine sand paper, rinsed with water, degreased by acetone, etched in HNO_3 (1:3) solution, and rinsed thoroughly with water. The slurry of the active materials was left to relatively dry to obtain a slurry paste. The resulting paste was supported on the graphite plates of 1 cm^2 area and then heated to 60 °C in an oven for 24 h. The electrodes contained ≈ 1.29 mg of the active material. The electrodes were pressed together using a crimper. A Pellon paper soaked in 0.05 mol L^{-1} KOH was used as a separator.

Table 1 A summary of ferrite-based electrode materials applied in supercapacitors

| Ferrite	Capacitance/F g^{-1}	Remark	References
PANI-NiFe$_2$O$_4$	442 (1 mA cm^{-2})	–	[30]
NiFe$_2$O$_4$	454 (0.1 A g^{-1})	Average crystallite size of 34 nm	[32]
PEDOT	156 (1 mA cm^{-2})	Nanotube structure	[33]
NiFe$_2$O$_4$	127 (1 mA cm^{-2})	A size of 5–20 nm	[33]
PEDOT-NiFe$_2$O$_4$	251 (1 mA cm^{-2})	Nanocomposites	[33]
Ni$_{0.8}$Zn$_{0.2}$Fe$_2$O$_4$	19 (20 mV s^{-1})	Synthesis by electrodeposition	[34]
NiFe$_2$O$_4$	196 (5 A g^{-1})	Composite with graphene	[35]
NiFe$_2$O$_4$	18.5 (10 mV s^{-1})	In 1 mol L^{-1} LiClO$_4$, 0.1~0.8 μm particle size	[36]
MnFe$_2$O$_4$	97.1 (0.1 A g^{-1})	Colloidal nanocrystal clusters	[37]
MnFe$_2$O$_4$	93.9 (0.1 A g^{-1})	Colloidal nanocrystal clusters	[37]
MnFe$_2$O$_4$	74.2 (0.1 A g^{-1})	Colloidal nanocrystal clusters, LiOH electrolyte	[37]
MnFe$_2$O$_4$	47.7 (0.1 A g^{-1})	Colloidal nanocrystal clusters, Na$_2$SO$_4$ electrolyte	[37]
MnFe$_2$O$_4$	221 (50 mV s^{-1})	Composites with graphene and CNT	[38]
MCBP	204.3 (0.5 A g^{-1})	Nanoparticles of 8 nm	[39]
MCB	26.8 (0.5A g^{-1})	Nanoparticles of 8 nm	[39]
MnFe$_2$O$_4$	53.3 (0.05 A g^{-1})	Colloidal Nanocrystal Cluster 5 nm	[40]
MnFe$_2$O$_4$	99 (4 mV s^{-1})	Nanocrystals of 13 nm	[41]
LiMn$_2$O$_4$	128 mA h g^{-1} (0.074 A g^{-1})	Spinel crystals of 1 μm	[41]
MnFe$_2$O$_4$	300 (0.3 A g^{-1})	MnFe$_2$O$_4$/graphene hybrid inks	[42]
MnFe$_2$O$_4$	115 (20 mV s^{-1})	Nanocrystals of 13.2 nm	[43]
NiZnFe$_2$O$_4$	67 (20 mV s^{-1})	Nanoflakes of 80–90 nm	[45]
CoFe$_2$O$_4$	123.2 (5 mA cm^{-2})	RGO composite	[47]
CoFe$_2$O$_4$	21.1 (5 mA cm^{-2})	GO composite	[47]
CoFe$_2$O$_4$	18.7 (5 mA cm^{-2})	–	[47]
CoFe$_2$O$_4$	366 (5 mV s^{-1})	Nanoflakes-like morphology	[48]
CoFe$_2$O$_4$	99 (10 mV s^{-1})	400 nm with nanorod shape	[49]
CoFe$_2$O$_4$	195 (10 mV s^{-1})	300 nm with nanoring shape	[49]
CuFe$_2$O$_4$	47 (10 mV s^{-1})	Nanowire composite	[50]
MWCNTs-CuFe$_2$O$_4$	115 (10 mV s^{-1})	Ferrite of nanorod shape attached to MWCNTs	[50]
FMWCNTs-CuFe$_2$O$_4$	267 (10 mV s^{-1})	Fluorinated MWCNTs	[50]
CuFe$_2$O$_4$-graphene	576.6 (0.1 A g^{-1})	–	[51]
CuFe$_2$O$_4$	5.7 (0.3 μA cm^{-2})	Spray-pyrolyzed thin film	[52]
CuFe$_2$O$_4$	72 (100 mV s^{-1})	Nanocrystals of 80 nm	[53]
CuCoFe$_2$O$_4$	397 (0.1 A g^{-1})	Nanocomposite, KOH electrolyte	[55]
Al$_{0.2}$Cu$_{0.4}$Co$_{0.4}$Fe$_2$O$_4$	540 (0.1 A g^{-1})	Nanocomposite	[55]
Al$_{0.4}$Cu$_{0.3}$Co$_{0.3}$Fe$_2$O$_4$	487 (0.1 A g^{-1})	Nanocomposite	[55]
Al$_{0.6}$Cu$_{0.2}$Co$_{0.2}$Fe$_2$O$_4$	315 (0.1 A g^{-1})	Nanocomposite	[55]
Al$_{0.8}$Cu$_{0.1}$Co$_{0.1}$Fe$_2$O$_4$	256 (0.1 A g^{-1})	Nanocomposite	[55]
BiFeO$_3$	72.7 (0.1 A g^{-1})	Electrodeposited BiFeO$_3$	[56]
MnFe$_2$O$_4$	125 (0.1 A g^{-1})	EC/EMC/LiPF$_6$ electrolyte	[57]
LiFeO$_2$	45 (10 mV s^{-1})	Rounded shape of 80 nm, 144 m^2 g^{-1} surface area	[58]
CoFe$_2$O$_4$	854 mA h g^{-1} (0.1 mA cm^{-2})	Nanoparticles of 40 nm	[59]
Ni$_x$Mn$_{1-x}$Fe$_2$O$_4$	147, 120, 131, 185 (5 mV s^{-1})	x = 0.2, 0.4, 0.6, 0.8, 1 mol L^{-1} KOH	[60]
MnFe$_2$O$_4$	55 (200 mV s^{-1})	A 1:1 composite with carbon black	[61]
ZnMnFe$_2$O$_4$	77.9	30 nm, KOH electrolyte	This work

MCBP manganese ferrite/carbon black/poly(aniline), *MCB* manganese ferrite/carbon black, *PEDOT* poly(3-4ethylenedioxythiophene)

Results and discussion

Figure 1a, b shows FESEM images of ZMFNPs with two different magnifications. ZMFNPs are appeared as spherical nanoparticles of 30.7 ± 3.7 nm ($n = 100$). There are also some agglomerations related to the magnetic entity of the nan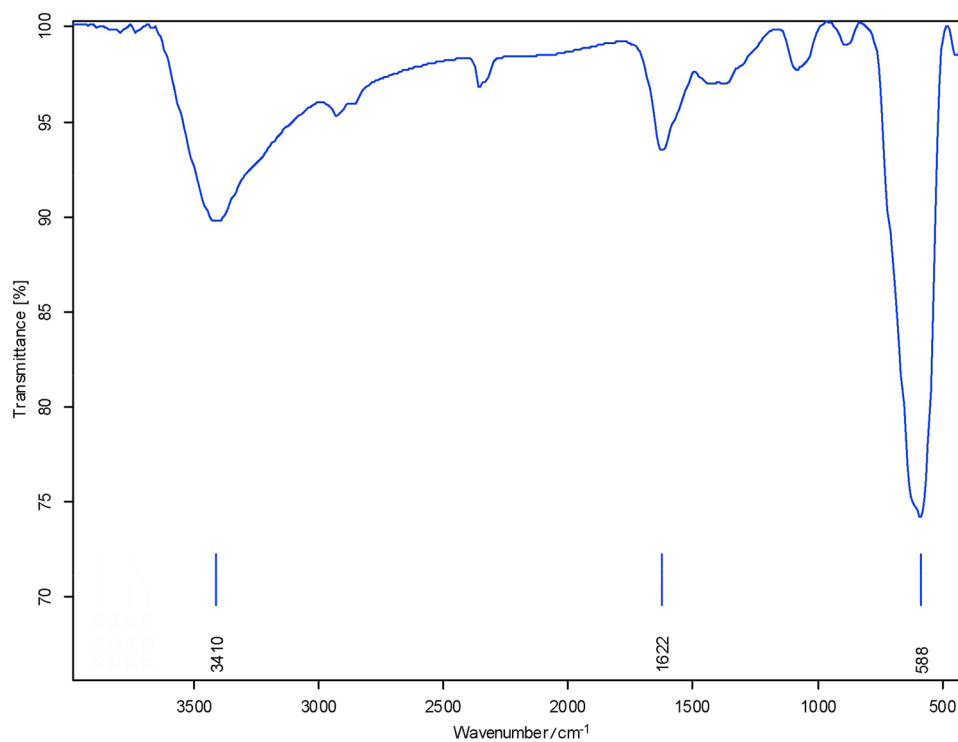oparticles. It should be noted that because the FESEM images were recorded from a dried ZMFNPs sample, the agglomerations were occurred. Figure 1c shows an energy-dispersive X-ray spectrum of ZMFNPs confirming the presence of the constituent elements with the respective stoichiometry.
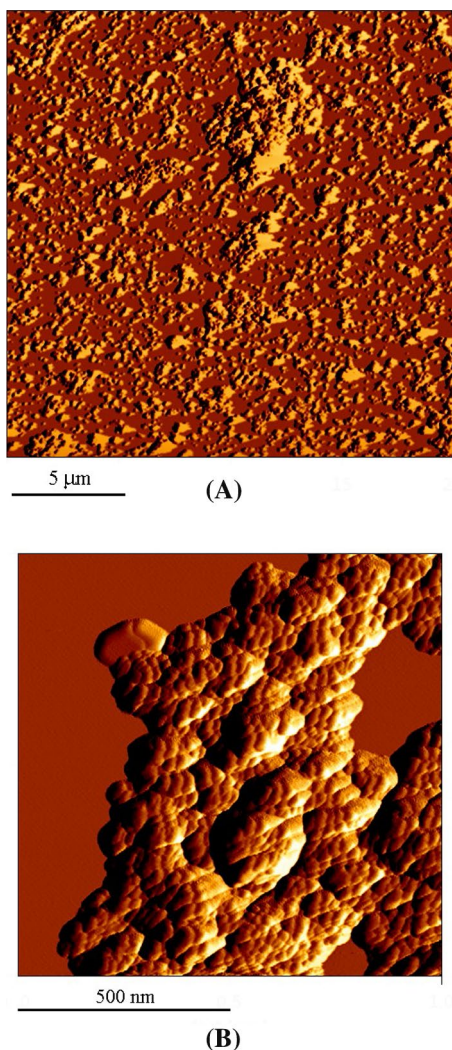
A FTIR spectrum of ZMFNPs is presented in Fig. 2. The peak appeared at 588 cm^{-1} is related to the intrinsic
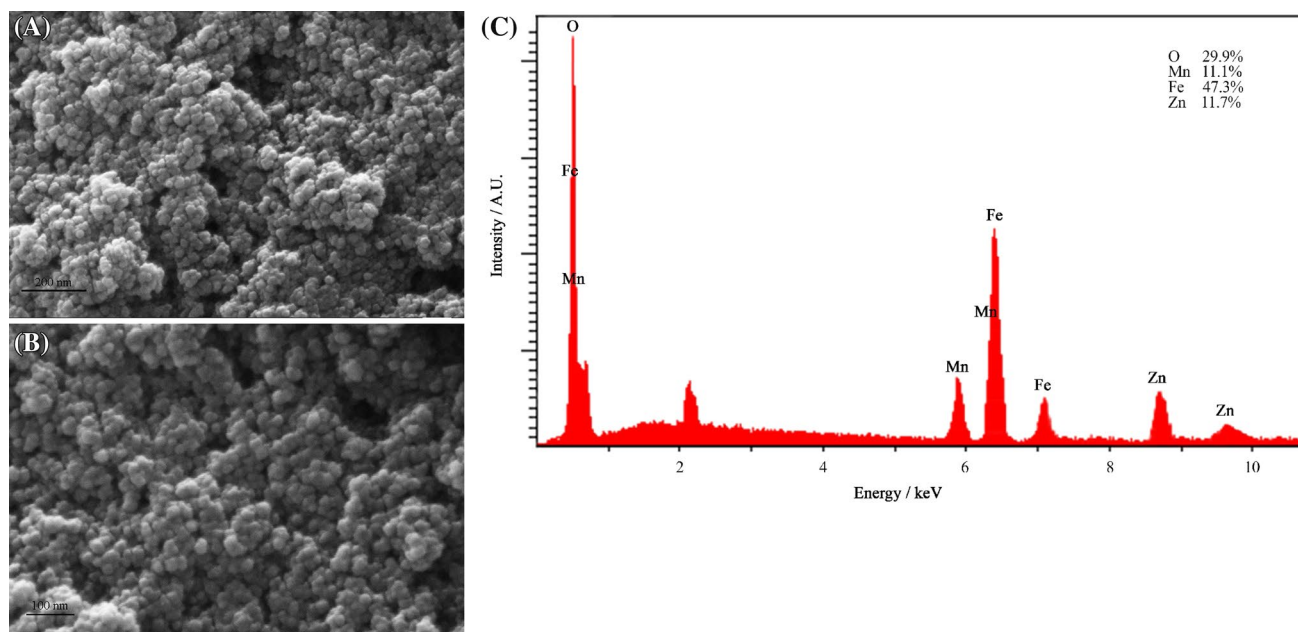
Fig. 1 FESEM images at two different magnifications (**a, b**), and an energy-dispersive X-ray spectrum of ZMFNPs

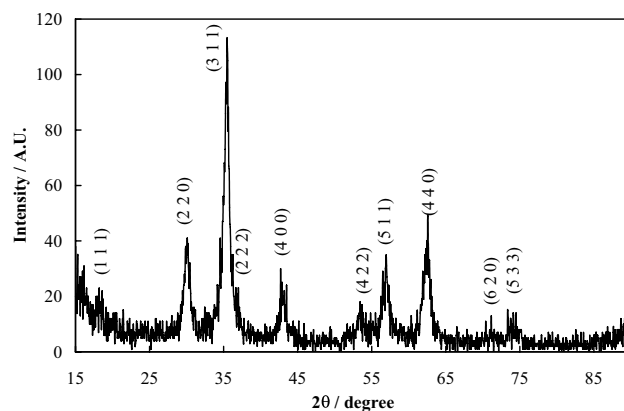**Fig. 2** FTIR spectrum of ZMFNP nanoparticle

(A)

(B)

Fig. 3 AFM images of ZMFNPs in two different magnifications

Fig. 4 An XRD pattern of the ZMFNP nanoparticle

Fig. 5 Cyclic voltammograms of the GC, GC/AB and NC electrodes
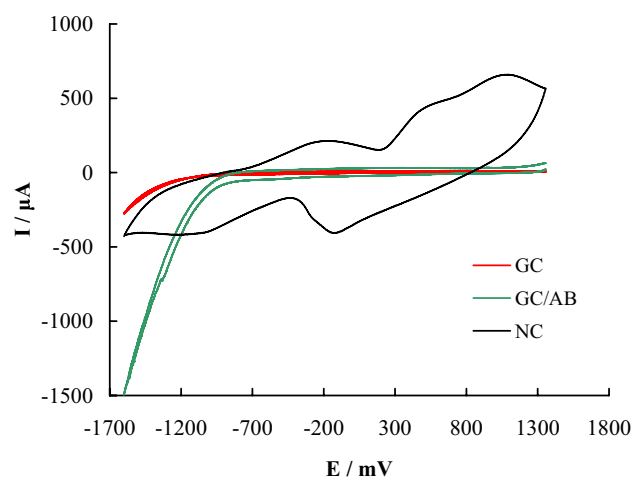
stretching vibration of tetrahedral groups $Fe^{3+} O^{2-}$ of spinel ferrite structures [62]. Bands at 1622 and 3410 cm^{-1} are related to OH stretching vibration from adsorbed hydroxyl group and water molecules adsorbed from surrounding, respectively [63].

AFM images from ZMFNPs with two different magnifications are shown in Fig. 3. The images confirm the morphological results obtained from FESEM, and provide a particle size of 29.8 ± 4.9 nm ($n = 50$).

An XRD pattern for ZMFNPs is shown in Fig. 4. The spectrum contains some main peaks at 2θ of about 18.4°, 30.0°, 35.5°, 36.8°, 42.7°, 53.8°, 56.7°, 62.4°, 71.5° and 74.5°. The pattern of the diffractogram is according to the manganese ferrite (JCPDS card number 38–0430) with some broadening in the peaks due to the small size of ZMFNPs. The diffraction peaks are assigned to (1 1 1), (2 2 0), (3 1 1), (2 2 2), (4 0 0), (4 2 2), (5 1 1), (4 4 0), (6 2 0) and (5 3 3) reflection planes, respectively. In addition,

the mean crystalline size of ZMFNPs was obtained as 9.89 ± 1.34 nm using the full width at half maximum of diffraction peaks and the Scherrer equation.

In Fig. 5, cyclic voltammograms of the GC, GC/AB and NC electrodes are presented. While voltammograms of the GC and GC/AB electrodes contained no redox peak with very low charging currents, the NC electrode bore multiple redox peaks with the highest charging current. The redox reactions in the voltammograms of the NC electrode are attributed to the both manganese and iron entities in the ZMFNPs structure accompanied by insertion/deinsertion of hydrogen ions according the following semi-reactions [43, 64]:

$$2Zn_{0.5}Mn_{0.5}Fe_2O_4 + 4H_2O \rightleftarrows Zn(OH)_2 + MnOOH \\ + 4FeOOH + H^+ + e, \tag{1}$$

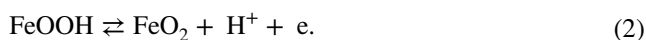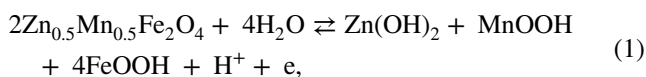$$FeOOH \rightleftarrows FeO_2 + H^+ + e. \tag{2}$$

Figure 6 shows cyclic voltammograms of the NC electrode recorded in KOH solutions of different concentrations. Based on the results, the highest (both Faradaic and charging) currents were measured in the concentration of 0.05 mol L^{-1} and it was selected for further studies. Based on the results, the conductivity of the electrolyte had minor effect on the supercapacitive behavior of the NC electrode, and lower currents in the voltammograms recorded at higher concentrations of KOH solutions can be related to dissolution of the active material [65].

Nyquist diagrams recorded for the GC and GC/AB and the NC electrodes at open circuit potential are shown in Fig. 7. In the diagrams, the GC electrode present two depressed semicircles in the entire range of the swept frequency related to the negligible redox reactions occur at
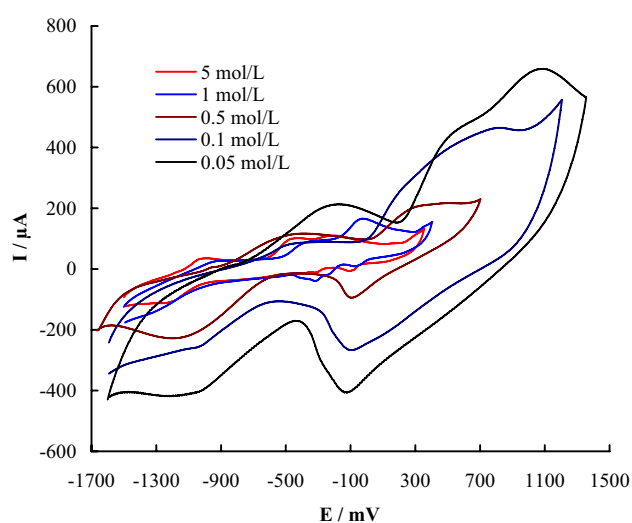
Fig. 6 Cyclic voltammograms of the NC electrode in different concentrations of KOH
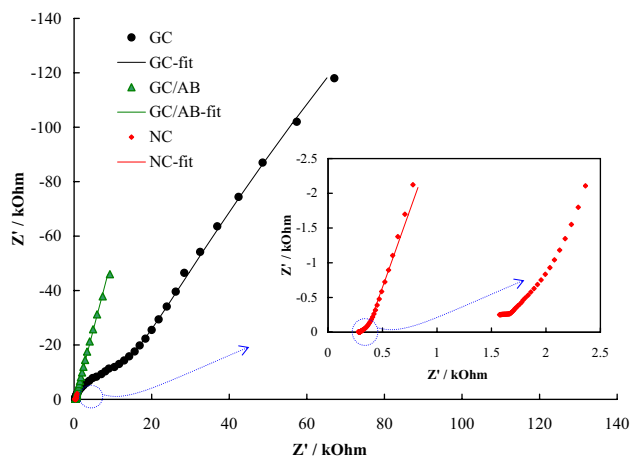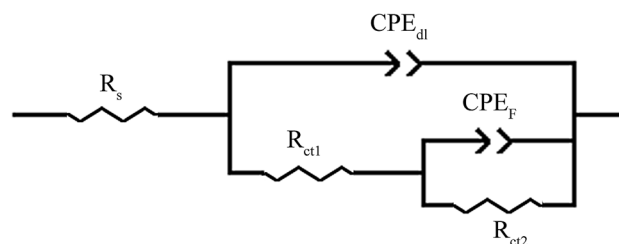

Fig. 7 Nyquist diagrams of the GC, GC/AB and NC electrodes at open circuit potential

carbonaceous surfaces of oxygen functional groups. Similarly, the GC/AB electrode represents similar signature with a higher rate due to the higher active area of acetylene black. In the Nyquist diagram recorded for the NC electrode, a highly depressed semicircle was appeared at high frequencies, following by an open Warburg signature. The high-frequency semicircle is related to the redox reactions (Eqs. 1 and 2) which the high porosity of the NC electrode surface causes to energy dissipation in the double layer capacitance. The open Warburg behavior is a typical ideal capacitors with a limitation in the diffusion of (most probably hydronium) ions into the ferrite lattice. For the Nyquist diagrams recorded for the GC and GC/AB electrodes, an equivalent electrical circuit shown in Scheme 1, and for the Nyquist diagram recorded for the NC electrode, an equivalent electrical circuit presented in Scheme 2 is proposed. In these circuits, R_s, CPE_{dl} and R_{ct} represent ohmic solution resistance, a constant phase element for the double layer capacitance, and charge transfer resistance of the redox reaction(s). Combination of R_{ct} and CPE_F characterizes the low-frequency semicircle in the Nyquist diagrams of the GC and GC/AB electrodes. W_O represents an open circuit terminus finite length Warburg element with an impedance of [66]:

$$Z_{Wo} = [R_W \text{ctnh}(T_W j\omega)^n] / (T_W j\omega)^n, \tag{3}$$

where T_W and n are the Warburg coefficient and Warburg coefficient exponent, respectively. $R_W = l^2/D$, where l and D are the effective diffusion length and coefficient, respectively. The values of the circuit elements in the equivalent circuits of Schemes 1 and 2 obtained by fitting on the experimental Nyquist diagrams are presented in Table 2. Using the


Scheme 1 Equivalent electrical circuit of Nyquist diagrams for the GC and GC/AB electrodes
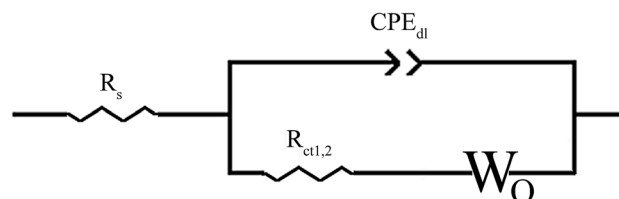
Scheme 2 Equivalent electrical circuit of Nyquist diagrams of the NC electrode

Table 2 Values of the circuit elements in the equivalent circuits presented in Schemes 1 and 2 obtained by fitting on the experimental Nyquist diagrams

Electrode	R_s/Ω	CPE_{dl}		R_{ct1}/Ω	CPEF		$R_{ct2}/M\Omega$
		$T/\propto\Omega^{-1}\,s^n$	n		$T/\propto\Omega^{-1}\,s^n$	n	
GC	271.2 (0.2%)	6.36 (0.74%)	0.93 (0.15%)	18,733 (1.13%)	26.5 (0.38%)	0.75657 (0.6%)	1.69 (13.2%)
GC/AB	175.5 (fixed)	17.5 (17%)	0.82 (fixed)	75.0 (fixed)	7.96 (fixed)	0.90 (fixed)	7.96 (3.49%)

Electrode	R_s/Ω	CPE_{dl}		R_{ct1}/Ω	Electrode	W_O		
		$T/\propto\Omega^{-1}\,s^n$	n			R_W/Ω	$T_W/\Omega^{-1}\,s^n$	n_W
NC	–	–	–	–		226.8 (3.45%)	0.47 (4.61%)	0.43 (0.41%)
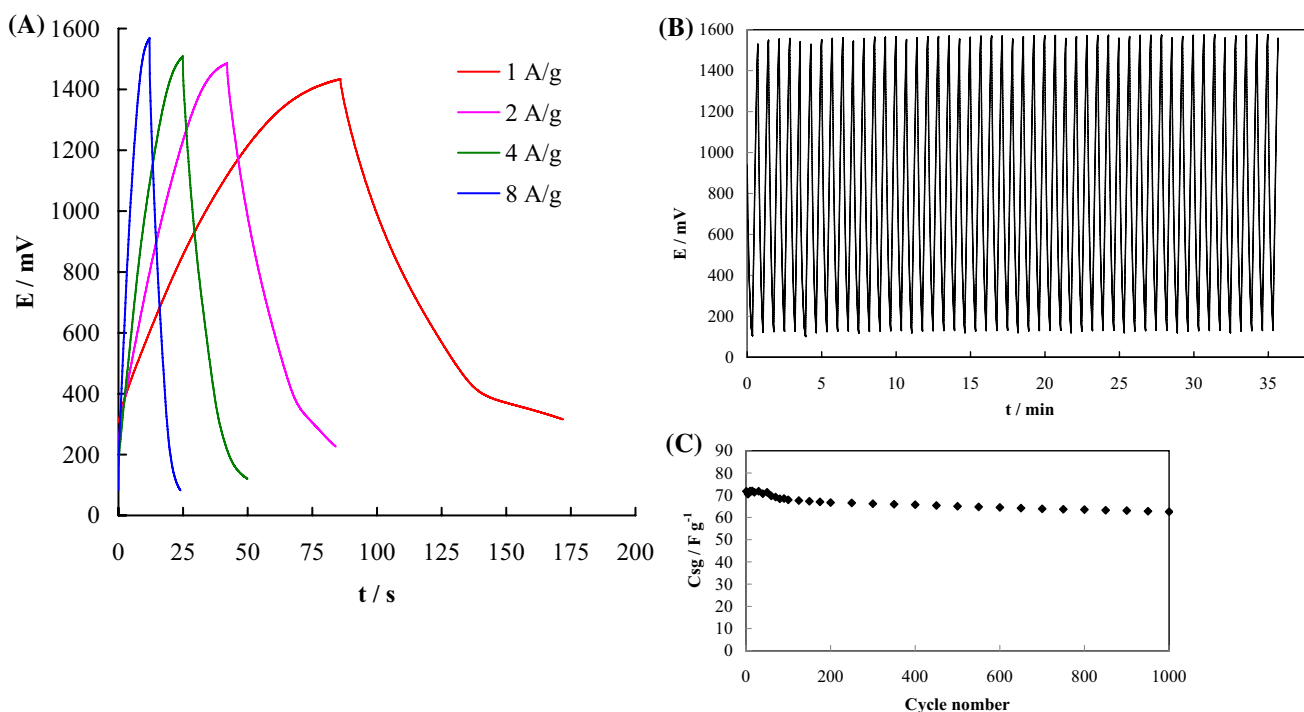
Fig. 8 **a** Galvanostatic charge/discharge curves of the NC electrode at different current densities. **b** Galvanostatic charge/discharge cycles of the NC electrode at 8 A g^{-1} current density. **c** Specific capacitance changes of the NC electrode in charge/discharge cycles

values of R_W for the NC electrode and the particles size of ZMFNPs as the diffusion thickness, the values of the diffusion coefficient of hydrogen ion in ZMFNPs were obtained as $(4.16\times10^{-14}\pm0.06)$ cm^2 s^{-1},

Figure 8a shows typical galvanostatic charge/discharge curves for the NC electrode at different current densities. The specific capacitance of the NC electrode was obtained using the following equation:

$$C_{Sg} = I\,\Delta t\,/\,4\,m\,\Delta V, \tag{4}$$

where C_{Sg} is the specific capacitance, I is the current, Δt is the discharge time, ΔV is the potential change during the charge/discharge process, and m is the mass of the active material of a single electrode. A coefficient of 1/4 is inserted

in Eq. 4 because in the symmetric two-electrode cell, two similar capacitors are placed in series with two-time active mass, compared to the three-electrode cell. The maximum specific energy of the NC electrode was obtained using the following equation:

$$E_{Sg} = 0.5\,C_{Sg}\Delta V^2/\,3.6. \tag{5}$$

The values of C_{Sg} and E_{Sg} obtained from the galvanostatic charge/discharge curves are reported in Table 3. A comparison of the specific capacitance of some ferrites employed as supercapacitor electrode materials is also made in Table 1.

The stability of the NC electrode was evaluated by subjecting to 1000 galvanostatic charge/discharge cycles at

Table 3 The specific capacitance of NC at different current densities

Current density/A g^{-1}	Specific capacitance/F g^{-1}	Specific energy/Wh g^{-1}
1	77.9	13.2
2	71.0	14.7
4	74.1	18.4
8	71.8	17.6

a current density of 8 A g^{-1} and the results are shown in Fig. 8b. Figure 8c shows changes in C_{Sg} as a function of cycle number indicating a little decrement in the specific capacitance of the NC electrode during consecutive charge/discharge cycles. C_{Sg} retains > 87% of the initial value after 1000 cycles.

Conclusion

In summary, ZMFNPs were successfully synthesized through a facile low-cost chemical reaction. The proposed method can be extended and applied for the synthesis of other substituted ferrite nanomaterials. The nanoparticles showed some redox transitions in a 0.05 mol L^{-1} KOH electrolyte in an operating potential window of 150–1570 mV with a high charging current providing a good supercapacitor electrode material.

References

1. P. Simon, Y. Gogotsi, Nat. mater. **7**, 845 (2008)
2. L.x. Feng, L.G. Ren, T.Y. Xiang, Sci. China Technol. Sci. **58**, 1799 (2015)
3. S.G. Kandalkar, D.S. Dhawale, C.K. Kim, C.D. Lokhande, Synth. Met. **160**, 1299 (2010)
4. C. Liu, F. Li, L.P. Ma, H.M. Cheng, Adv. Mater. **22**, E28 (2010)
5. L. Shiri, N. Sattarahmady, H. Heli, J. Electroanal. Chem. **719**, 143 (2014)
6. H. Heli, A. Parsa, N. Sattarahmady, J. Electroanal. Chem. **751**, 15 (2015)
7. H. Heli, H. Yadegari, A. Jabbarib, Mater. Chem. Phys. **134**, 21 (2012)
8. V. Augustyn, P. Simon, B. Dunn, Energy Environ. Sci. **7**, 1597 (2014)
9. T. Brezesinski, J. Wang, S.H. Tolbert, B. Dunn, J. Sol–Gel. Sci. Technol. **57**, 330 (2011)
10. M.Y. Ho, P.S. Khiew, D. Isa, T.K. Tan, W.S. Chiu, C.H. Chia, Nano **09**, 1430002 (2014)
11. G.A. Snooka, P. Kaob, A.S. Best, J. Power Sources **196**, 1 (2011)
12. S. Ghosh, O. Inganäs, Adv. Mater. **11**, 1167 (1999)
13. N. Sattarahmady, A. Parsa, H. Heli, J. Mater. Sci. **48**, 2346 (2013)
14. N. Sattarahmady, R.D. Vais, H. Heli, J. Appl. Electrochem. **45**, 577 (2015)
15. J. Li, X. Cheng, A. Shashurin, M. Keidar, Graphene **1**, 1 (2012)
16. H. Yadegari, H. Heli, A. Jabbari, J. Solid State Electrochem. **17**, 2203 (2013)
17. H. Heli, H. Yadegari, J. Electroanal. Chem. **713**, 103 (2014)
18. R.C. Pullar, Prog. Mater. Sci. **57**, 1191 (2012)
19. D.S. Mathew, R.S. Juang, Chem. Eng. J. **129**, 51 (2007)
20. N. Sattarahmady, M. Heidari, T. Zare, M. Lotfi, H. Heli, Appl. Magn. Reson. **47**, 925 (2016)
21. S. Rana, A. Gallo, R.S. Srivastava, R.D.K. Misra, Acta Biomater **3**, 233 (2007)
22. R. Ito, Y. Machida, T. Sannan, T. Nagai, Int. J. Pharm. **61**, 109 (1990)
23. N. Sattarahmady, N. Azarpira, A. Hosseinpour, H. Heli, T. Zare, J. Drug Deliv. Sci. Technol. **36**, 68 (2016)
24. H. Heli, N. Sattarahmady, G.R. Hatam, F. Reisi, R.D. Vais, Talanta **156–157**, 172 (2016)
25. P.P. Hankare, R.P. Patil, K.M. Garadkar, R. Sasikala, B.K. Chougule, Mater. Res. Bull. **46**, 447 (2011)
26. J.H. Nam, Y.H. Joo, J.H. Lee, J.H. Chang, J.H. Cho, M.P. Chun, B.I. Kim, J. Magn. Magn. Mater. **321**, 1389 (2009)
27. L. Cui, P. Guo, G. Zhang, Q. Li, R. Wang, M. Zhou, L. Ran, X.S. Zhao, Colloids Surf. A **423**, 170 (2013)
28. K.E. Farley, A.C. Marschilok, E.S. Takeuchi, K.J. Takeuchi, Electrochem. Solid-State Lett. **15**, A23 (2012)
29. L. Feng, Y. Zhu, H. Ding, C. Ni, J. Power Sources **267**, 430 (2014)
30. B. Senthilkumar, K.V. Sankar, C. Sanjeeviraja, R.K. Selvan, J. Alloys Compd. **553**, 350 (2013)
31. W. Wang, Q. Hao, W. Lei, X. Xia, X. Wang, J. Power Sources **269**, 250 (2014)
32. V. Venkatachalam, R. Jayavel, Solid state physics AIP conference proceeding 1665, 140016-1 (2015)
33. P. Sen, A. De, Electrochim. Acta **55**, 4677 (2010)
34. D.K. Pawar, S.M. Pawar, P.S. Patil, S.S. Kolekar, J. Alloys Compd. **509**, 3587 (2011)
35. E.K. Heidari, A. Ataie, M.H. Sohi, J.K. Kim, J. Ultrafine Grained Nanostruc. Mater. **48**, 27 (2015)
36. B. Senthilkumar, R.K. Selvan, P. Vinothbabu, I. Perelshtein, A. Gedanken, Mater. Chem. Phys. **130**, 285 (2011)
37. R. Wang, Q. Li, L. Cheng, H. Li, B. Wang, X.S. Zhao, P. Guo, Colloids Surf. A **457**, 94 (2014)
38. B. Li, Y. Fu, H. Xia, X. Wang, Mater. Lett. **122**, 193 (2014)
39. D. Zha, P. Xiong, X. Wang, Electrochim. Acta **185**, 218 (2015)
40. B. Wang, P. Guo, H. Bi, Q. Li, G. Zhang, R. Wang, J. Liu, X.S. Zhao, Int. J. Electrochem. Sci. **8**, 8966 (2013)
41. Y.P. Lin, N.L. Wu, J. Power Sources **196**, 851 (2011)
42. W. Cai, T. Lai, W. Dai, J. Ye, J. Power Sources **255**, 170 (2014)
43. S.L. Kuo, J.F. Lee, N.L. Wu, J. Electrochem. Soc. **154**, A34 (2007)
44. Shanmugavani, R.K.Selvan, RSC Adv. **4**, 27022 (2014)
45. D.K. Pawar, J.S. Shaikh, B.S. Pawar, S.M. Pawar, P.S. Patil, S.S. Kolekar, J. Porous Mater. **19**, 649 (2012)
46. Shanmugavani, D.Kalpana, R.K.Selvan, Mater. Res. Bull. **71**, 133 (2015)
47. P. Hez, K. Yang, W. Wang, F. Dong, L. Du, Y. Deng, Russ. J. Electrochem. **49**, 359 (2013)
48. V.S. Kumbhar, A.D. Jagadale, N.M. Shinde, C.D. Lokhande, App. Surf. Sci. **259**, 39 (2012)
49. D.H. Deng, H. Pang, J.M. Du, J.W. Deng, S.J. Li, J. Chen, J.S. Zhang, Cryst. Res. Technol. **47**, 1032 (2012)
50. S. Giri, D. Ghosh, A.P. Kharitonov, Ch.K. Das, Funct. Mater. Lett. **5**, 1250046 (2012)
51. W. Zhang, B. Quan, Ch Lee, S.K. Park, X. Li, E. Choi, G. Diao, Y. Piao, ACS Appl. Mater. Interfaces **7**, 2404 (2015)

52. D. Ham, J. Chang, S.H. Pathan, W.Y. Kim, R.S. Mane, B.N. Pawar, O.S. Joo, H. Chung, M.Y. Yoon, S.H. Han, Curr. Appl. Phys. 9, S98 (2009)
53. M.R. Kale, N.P. Tendolkar, Int. J. Sci. Eng. Res. **4**, 12 (2013)
54. Rai, A.L. Sharma, A.K. Thakur, Solid State Ionics **262**, 230 (2014)
55. Bhujunn, M.T.T. Tan, A.S. Shanmugam, Ceram. Int. **42**, 6457 (2016)
56. V.V. Jadhav, M.K. Zate, Sh Liu, M. Naushad, R.S. Mane, K.N. Hui, S.H. Han, Appl. Nanosci. **6**, 511 (2016)
57. N.L. Wu, Y.H. Chen, ECS Trans. **16**, 223 (2008)
58. J.S. Pena, O. Crosnier, T. Brousse, Electrochim. Acta **55**, 7511 (2010)
59. L.J. Li, Sol–Gel Sci. Technol. 58, 677 (2011)
60. M.K. Zate, S.M.F. Shaikh, V.V. Jadhav, K.K. Tehare, S.S. Kolekar, R.S. Mane, M. Naushad, B.N. Pawar, K.N. Hui, J. Anal. Appl. Pyrolysis **116**, 177 (2015)
61. S.L. Kuo, N.L. Wu, J. Power Sources **162**, 1437 (2006)
62. M. Gotic, I.C. Nagy, S. Popovic, S. Music, Philos. Mag. Lett. **78**, 193 (1998)
63. Z. Tang, P. Liu, J. Guo, Z. Su, C. Yang, Appl. Surf. Sci. **255**, 2125 (2008)
64. M. Zhu, D. Meng, C. Wang, G. Diao, ACS Appl. Mater. Interfaces **5**, 6030 (2013)
65. D.A. Palmer, L.M. Anovitz, J. Solut. Chem. **38**, 869 (2009)
66. E. Barsoukov, J. Ross Macdonald, *Impedance Spectroscopy Theory Experiment and Applications*, 2nd edn. (Wiley, Hoboken, 2005)